Available online at www.sciencedirect.com

ScienceDirect

Advances in Space Research xxx (xxxx) xxx

ADVANCES IN SPACE RESEARCH (a COSPAR publication)

www.elsevier.com/locate/asr

Spectral changes of the NWA 10580 meteorite under simulated space weathering: Insights from VIS–NIR and microXRD analyses

Ákos Kereszturi [a,c,*], Ildikó Gyollai [b], Sándor Biri [d], Zoltán Juhász [d], Bernadett D. Pál [a,c], Richárd Rácz [d], Dániel Rezes [a,c], Béla Sulik [d], Máté Szabó [b,c], Péter Szávai [c,e], Zoltán Szalai [c,e,f]

[a] *Konkoly Thege Miklos Astronomical Institute HUN-REN Research Centre for Astronomy and Earth Sciences, Konkoly Thege Miklos ut 15-17, Budapest H-1121, Hungary*

[b] *Institute for Geological and Geochemical Research, HUN-REN Research Centre for Astronomy and Earth Sciences, Budapest H-1112, Hungary*

[c] *MTA Centre of Excellence, Research Centre for Astronomy and Earth Sciences, Konkoly Thege Miklos ut 15-17, Budapest H-1121, Hungary*

[d] *HUN-REN Institute for Nuclear Research, Debrecen, H-4016, Hungary*

[e] *Geographical Institute, HUN-REN Research Centre for Astronomy and Earth Sciences, Budapest H-1112, Hungary*

[f] *Department of Environmental and Landscape Geography, ELTE, Budapest H-1117, Hungary*

Received 4 June 2025; received in revised form 4 November 2025; accepted 19 November 2025

Abstract

We investigate the effects of space weathering on asteroid surfaces by exposing the NWA 10580 meteorite to 1 keV solar wind proton irradiation, with a total fluence of up to 10^{17} ions/cm^2, equivalent to ~10 Myr of exposure in space. We collect pre- and post-irradiation spectra using near-infrared spectroscopy and micro-X-ray diffraction. We observed irradiation-induced amorphization, reflected in systematic shifts in d-spacing and peak broadening of crystalline phases. Orthopyroxene and carbonates showed an increasing d-spacing consistent with previous studies, while olivine exhibited changes associated with magnesium loss. Pyroxene spectra revealed the disappearance of minor absorption bands. In some cases, irregular d-spacing variations suggest metastable effects linked to pre-existing defects. These results improve our understanding of mineralogical evolution under space weathering, support the interpretation of asteroid spectral data in future missions and the development of spectral detectors. Comparing the pristine samples with the ones exposed to the highest irradiation level, the largest peak position shift was observed for the olivine 835 nm band (14 nm), whereas the pyroxene band at 1938 nm showed the smallest variation (1 nm). In terms of FWHM, the pyroxene band at 1938 nm and the OH band exhibited the most pronounced broadening (93 nm and 65 nm), while the olivine bands at 835 nm and 860 nm showed only minor changes (6 nm and 10 nm). These results could be used and applied for the selection of band positions for small, low cost infrared detectors onboard future cubesat missions.

Keywords: Meteorite; Spectroscopy; Near-infrared; Space weathering; NWA10580; Irradiation

1. Introduction

Space weathering processes alter the surfaces of airless solar system bodies, complicating the spectral interpretation of asteroid observations. Asteroid surfaces generally exhibit a feature poor spectra compared to those of mete-

* Corresponding author at: Konkoly Thege Miklos Astronomical Institute HUN-REN Research Centre for Astronomy and Earth Sciences, Konkoly Thege Miklos ut 15-17, Budapest H-1121, Hungary.

E-mail address: kereszturi.akos@csfk.org (Á. Kereszturi).

https://doi.org/10.1016/j.asr.2025.11.086

Please cite this article as: Á. Kereszturi, I. Gyollai, S. Biri et al., Spectral changes of the NWA 10580 meteorite under simulated space weathering: Insights from VIS–NIR and microXRD analyses, Advances in Space Research, https://doi.org/10.1016/j.asr.2025.11.086

orites as the latter present a more feature-rich spectra (Moretti et al., 2007). Spectral differences such as these hinder the direct linking between meteorites and their parent asteroids (Chapman, 2004; de León et al., 2006), impeding efforts to reconstruct asteroid origins or to assess planetary defense strategies. From the analysis of space weathering effects on the infrared mineral bands of meteorites, we will better understand the composition of asteroids whose surfaces are heavily weathered. This work aims to contribute some new findings using one specific meteorite. The rationality of the jointly used infrared and XRD techniques is that while the first shows the appearance of the material (relevant to both meteorites and asteroids) the second shows their internal crystalline structure. The linkage between meteorites and asteroids has been improved by the separation of primary and secondary parent bodies, where the primary is the ultimate source of meteorites, while the secondary is another asteroid formed by the impact or break-up of the primary one (Greenwood et al., 2020). For example Vestoid asteroids and Vesta should be considered differently, as their spectra are similar; however, their meteorite ejection properties (including mass related gravity and orbital characteristics) are somewhat different: In the comprehensive study of Greenwood et al. (2020) 100–150 parent bodies are represented in the analysed meteorite collection, with the strongest or most readily identifiable links between HED meteorites and asteroid Vesta.

Space weathering includes a range of processes including solar and galactic particle irradiation, UV exposure, micrometeorite impacts (commonly referred to as meteoritic gardening), producing regolith mixing (Trigo-Rodríguez et al., 2022) and extreme thermal cycling (Delbo et al., 2014; Brunetto et al., 2015). Among these, ion irradiation – particularly from solar wind protons – is a primary agent of mineralogical and spectral alteration. Simulating this process in the laboratory helps isolate its specific effects and improves our ability to interpret asteroid spectra. It is also worth considering that thermal cycling-driven cracking affects material strength, as well as radiation-driven amorphisation, thus the ratio of these two factors and their relative contribution should be further evaluated.

In this study, we investigate mineralogical and spectral changes in the NWA 10580 carbonaceous chondrite (CO3) induced by sequential proton irradiation. We selected this meteorite due to its minimal terrestrial alteration and the availability of baseline measurements from prior studies performed by the authors (Gyollai et al., 2024). Artificial irradiation experiments were performed in three cumulative steps, and the sample was analyzed before and after each irradiation action using IR spectroscopy and micro-X-ray techniques.

Previous laboratory studies have established key irradiation-induced effects, here only the main and most frequently cited ones are listed. For example, ion bombardment has been shown to disordered carbonaceous materials and cause the amorphization of silicates (Brunetto et al., 2014; Baratta et al., 2010), and modifications of organics (Urso et al., 2020a). Brunetto et al. (2014) observed amorphization of olivine and dehydrogenation of organics in the Allende meteorite using He^{+} ions. Urso et al. (2020b) have demonstrated that accumulated irradiation dose influences the residue composition, and that astrophysical timescales are short enough to allow efficient formation of organic refractory materials on icy bodies in the outer Solar System. Similar effects include increased spectral darkening and reddening, band weakening, and structural damage – frequently attributed to the formation of nanophase iron (Keller and McKay, 1993; Pieters et al., 1993; Hapke, 2001; Sasaki et al., 2003; Kanuchova et al., 2015). However, a range of other changes also occur, depending on the original composition of meteorites, occasionally resulting in brightening and bluing (Lantz et al., 2017).

Observational evidence for irradiation effects also comes from sample return missions, which have revealed surface amorphization, variable oxidation states, and silicon enrichment in asteroid regoliths (Noguchi et al., 2011; Matsumoto et al., 2015; Matsumoto et al., 2016; Thompson et al., 2016). Studies of terrestrial analogs such as zircons have further shown that ion irradiation introduces crystal lattice defects, observable via Raman spectroscopy and band broadening and luminescence loss (Nasdala et al., 2010).

Despite these advances, gaps remain in our understanding of irradiation-induced transformations in meteorite minerals and organics, especially under controlled proton exposure. Some recent studies of Phobos simulant samples affected by micrometeorite bombardment have shown olivine decomposition, the emergence of nanophase iron, and melting of pyroxenes surfaces, while fluorescence was modified as the passivating effect of this nanophase iron increased (Weber et al., 2023). Peak width or FWHM (Full Width at Half Maximum) variations could be also linked to thermal metamorphism and not only to irradiation (Jakubek and Fries, 2022). Matsuoka et al. (2016) found that graphitization of organic matter under laser irradiation is more prominent in IR than in Raman spectra - however in this work no organics have been considered.

Building on this context, our study aims to quantify and characterize the progressive effects of artificial proton irradiation on the NWA 10580 sample, with a focus on Raman-observable mineralogical changes. These results will enhance interpretation of asteroid spectra and contribute to ongoing efforts to bridge the gap between meteorites and their parent bodies. Irradiation effects could also contribute to changes in the reflectance properties of carbonaceous chondrites and potential source asteroids (Tanbakouei et al., 2020), which may influence YORP effect related changes and warrant further analysis.

1.1. Current knowledge on meteorite-asteroid linking

The results detailed in this paper may have astrophysical and astronomical relevance in two key aspects: linking

asteroid spectra to meteorite spectra, and evaluating maturity related to space weathering, including ultraviolet and infrared spectra and bulk density (Moyano-Cambero et al., 2016) and reflectivity aspects (Tanbakouei et al., 2020; Trigo-Rodríguez et al., 2014). Among the consequences, darkening, reddening, and a suppression of absorption bands are most often observed and identified early at the Gaspra and Ida flybys (Helfenstein et al., 1994; Helfenstein et al., 1996). Regarding asteroid – meteorite connections, recent visual and near-infrared (VIS–NIR, ~200–2500 nm) studies, including findings from Hayabusa samples, support the connection between asteroids and meteorites through laboratory research. By jointly using meteorite measurements and dynamical models of asteroids (DeMeo et al., 2015), several links have been identified between meteorites and their source asteroids. Based on recent findings considering asteroid-meteorite links S-complex asteroids might represent pallasites, R-chondrites, brachinites and ordinary chondrites; while C–complex asteroids represent carbonaceous chondrites and impact melts; and X-complex asteroids represent also carbonaceous asteroids; while further asteroid types including T, D, O, R, V asteroid types according to Tholen classification represent ordinary chondrites, pallasites, brachinites. Using VIS–NIR and MIR (mid-infrared range, 2.5–25 μm) spectroscopy of weakly processed CO meteorites, a broad feature at 1.3 μm by iron-rich amorphous silicate matrix, the 21 μm feature of amorphous materials and glasses show a resemblance to asteroid (93) Minerva. While Minerva is not the only CO-like asteroid (e.g., Burbine et al. (2001)), it is likely the least-processed CO-like asteroid observed to date (McAdam et al., 2018). CO chondrites present good matches for K-types and Barbarian asteroids (Mahlke et al., 2023). Using isotopic evidences CO meteorites are linked to Eos family and K-type objects (Bell, 1988; Clark et al., 2009). The VIS–NIR reflectance of the S-type asteroid 25143 Itokawa (absorption features centered near 1.0 and 2.0 μm) indicates the presence of both olivine and pyroxene. While the spectra of some grains align with the ground-based observations both in spectral features and slope, some grains show a redder spectral slope (Abe et al., 2006). It showed resemblance to LL5 or LL6 chondrite meteorites. The difference is probably related to the variable extent of space weathering among the grains, influenced by varying amounts of nanophase metallic iron and FeS (Bonal et al., 2015).

The UV-NIR spectrum of the CH3 carbonaceous chondrite Pecora Escarpment 91467 (PCA 91467) shows similarities to that of asteroid (21) Lutetia (Trigo-Rodríguez et al., 2014; Moyano-Cambero et al., 2016), as evidenced by its slope, absolute reflectance, as well as the high metal content and reflectivity – features that are rare among carbonaceous chondrite (CC) meteorites. VIS–NIR reflectance analysis of Ryugu analogue mixtures suggests that several components (graphite, carbon, Mg-rich phyllosilicates and Fe-rich dark component) may be required to fit the asteroid spectra (Dirri et al., 2022). Additionally, further laser-induced weathering might be needed (Dirri et al., 2022) to reproduce micrometeoroid impacts, which produce amorphous layers and defect-rich olivine substrates (Fazio et al., 2017). Comparison of Ryugu samples analyzed in different wavelengths ranges show the link between CI carbonaceous chondrites and this asteroid (Kitazato et al., 2019; Yada et al., 2021; Pilorget et al., 2021), and are further supported by mineralogical analyses (Nakamura et al., 2023).

The analysis of the spectral role of Fe^{2+} in the VIS and NIR region of enstatite (including synthetic crystals) indicates a link between E-type asteroids and aubrites as well as enstatite chondrites. This connection is primarily supported by the 1 μm and 2 μm bands rather than the feature-poor VIS–NIR spectra (Markus et al., 2024). NIR (0.8–2.4 μm) spectroscopic observations after irradiation experiments indicated that the spectral slope of eucrites increases, altering their VIS–NIR spectra (0.4–2.5 μm). For NEAs, moderate space weathering effects may result from perturbations that expose unweathered surface grains (Fulvio et al., 2016).

Evaluating space weathering-related maturity may become feasible in the future, as the strength of various mineral peaks depends on the exposure. The so-called OMAT (Optical Maturity) parameter, developed for the Moon, numerically quantifies the regolith maturity. Over time, albedo and grain size decrease, spectra become redder, and absorption bands weaken (Lucey et al., 2000; Fischer and Pieters, 1994; Pieters et al., 1996; Noble et al., 2007). A similar parameter could potentially be developed for asteroids once we better understand the exposure duration required to create these changes. In this context, spectral reddening should be correlated with adsorption band weakening using artificial irradiation experiments, possibly complemented by laser-induced nanophase iron production. While a joint laboratory analysis of these two factors is difficult, it is not impossible and should be prioritized in the coming years.

2. Sample and methods

The NWA 10580 sample was studied using micro X-ray diffraction (microXRD) and VIS–NIR spectroscopy before and after three successive proton irradiation steps. Details of the sample, irradiation procedure, and experimental facilities are provided below. The locations of specific measurements were selected to be representative to the whole sample, however considering areal ratio, less than 1% of the total area was measured.

2.1. Sample

The NWA 10580 (CO3) meteorite sample used in this study what has been previously analysed already (Gyollai et al., 2024), was measured approximately in the form of a 4×3×1.5 mm and was cut to expose a flat, unpolished surface. It's mineralogical composition and petrological

characteristics – typical of a poorly altered Ornans-type carbonaceous chondrite – have been described in detail in Gyollai et al. (2024).

The VIS–NIR Shimadzu measurements were done on the bulk sample. The microXRD measurements were done at smaller, equivalent distinct areas with a diameter of 50–100 μm. The microXRD measurements were conducted on the same areas previously analyzed by FTIR in our earlier work (Gyollai et al., 2024), allowing a direct comparison of microXRD and VIS–NIR Shimadzu trends with the mid-infrared (MIR) results obtained earlier. The following measuring points were investigated at 12 areas: lower part of sample: A1 area (A1, A1 top, A1/3_4, A1/7_8), A2, A3, A4, A5; upper part of sample: B1, C1, D1, R1. During the calculation of spectral slopes, the recorded spectra were first normalized to unity at 550 nm. Then we used least-squares linear regression to fit the spectra between 200–700 nm. The resulting values were then multiplied by 10^4 to acquire the standard $\%/(10^3 Å)$ units (see Table 2.) in the Results section.

2.2. Irradiation

The sample was irradiated with 1 keV protons under vacuum conditions using the electron cyclotron resonance (ECR) ion source at the HUN-REN Institute for Nuclear Research (ATOMKI) (Biri et al., 2012). Three cumulative irradiation steps were applied: 15 s (10^{11} ion/cm^2 fluence) for the 1st irradiation, 1 h (10^{14} ion/cm^2 fluence) for the 2nd irradiation, and 1 day (10^{17} ion/cm^2 fluence) for the 3rd irradiation. These fluences represent the total number of incident protons per cm^2 of sample surface. In their study of the Allende meteorite, Brunetto et al. (2014) observed amorphization of olivine and dehydrogenation of organics under He^+ irradiation at fluences similar to our maximum dose (10^{17} ions/cm^2). The 1 keV energy was chosen based on measurements from the Ulysses and ACE satellites, which indicate that the majority of solar wind protons occur at this energy (Gloeckler, 2003). The highest fluence used in this study corresponds approximately to an average exposure time of $\sim 10^7$ years in space, though cumulative solar activity such as CMEs (coronal mass ejections) could further increase the dose. As the irradiations were cumulative, each step included the total proton input from all previous steps.

2.3. Used facilities

The sample was analyzed before and after each irradiation actions with microXRD and Shimadzu VIS–NIR spectrometers, targeting the same locations with XRD to record the modifications of the same minerals, that have been previously analyzed by Raman and infrared bulk measurements (Gyollai et al., 2024). The locations for analysis were identified using the optical microscopic image of the XRD instrument indicated below (marked with codes like B1, D1, A1, A3, R1/2, R1/11 etc., representing different points of the sample section, see Fig. 1). The XRD data are of minerals at each location are presented in the supporting online material with Tables SOM1/A-L and Figs. SOM2/A-L.

Shimadzu UV–vis-NIR (ultraviolet, visual, and near-infrared) 3600 spectrometer was used at the Institute for Geographical Research Centre for Astronomy and Earth Sciences (RCAES), HUN-REN in NIR (near-infrared) diffuse reflection mode. The detection records are in the range between 1.8 – 2.8 nm, with a spectral resolution of 0.1 nm, using a tungsten VIS–NIR light source. The equipment has 3 detectors: indium gallium arsenide (InGaAs), lead sulfide (PBS), photomultiplier tube (PMT). The peak identification of the recorded spectra was done by the Peak Pick Algorithm of the UVProbe software, which identifies any peak by the occurrence of 4 subsequent increasing values followed by 4 subsequent decreasing values. To properly select the real and obvious peaks, the Threshold (0.001) and Peak interval (0.01) adjustment parameters were used, and their performance confirmed by manual check. A sampling interval of 1 nm was applied during data screening, however, the indicated peak positions and FWHM values represent averages from one to two dozen different measurement locations of the same mineral type within the sample. During data interpretation pyroxene was identified according to Moriarty and Pieters (2016), the olivine was identified according to Pieters et al. (2008).

MicroXRD measurements were carried out at the Institute for Geological and Geochemical Research (HUN-REN) using a RIGAKU D/MAX RAPID II diffractometer (also used in e.g. Mozgai et al. (2019, 2021)). MicroXRD systems commonly employ 2D detectors such as imaging plates (IPs), charge-coupled devices (CCDs), complementary metal-oxide semiconductor (CMOS) chips, and position sensitive proportional counters (PSPCs). Curved detectors are optimized for a fixed sample-to-detector distance, while flat detectors allow variable distances, enabling a trade-off between spatial resolution and angular coverage. IPs offer the largest detection area among these technologies. The used RIGAKU instrument combines a MicroMax-003 third-generation microfocus sealed-tube X-ray generator with a curved IP detector, optimized for high-resolution, 2D diffraction analysis. The system operates with CuKα radiation at 50 kV and 0.6 mA, and supports a range of collimator sizes (10, 30, 50, 100, 300, 800 μm), allowing the irradiation area to be tailored according to the sample's dimensions. Sample alignment and selection of the measurement region are handled using a built-in CCD camera, position at a 45° angle for precise positioning.

During data collection, the curved IP detector – mounted on the inner wall of a cylindrical chamber centered on the ω-axis – records a 2D diffraction pattern across a wide 2θ range (double Bragg angle, calculated by the PDXL2 instrument according to the $n \times \lambda = 2d \times sin\theta$ formula, which indicates the angle

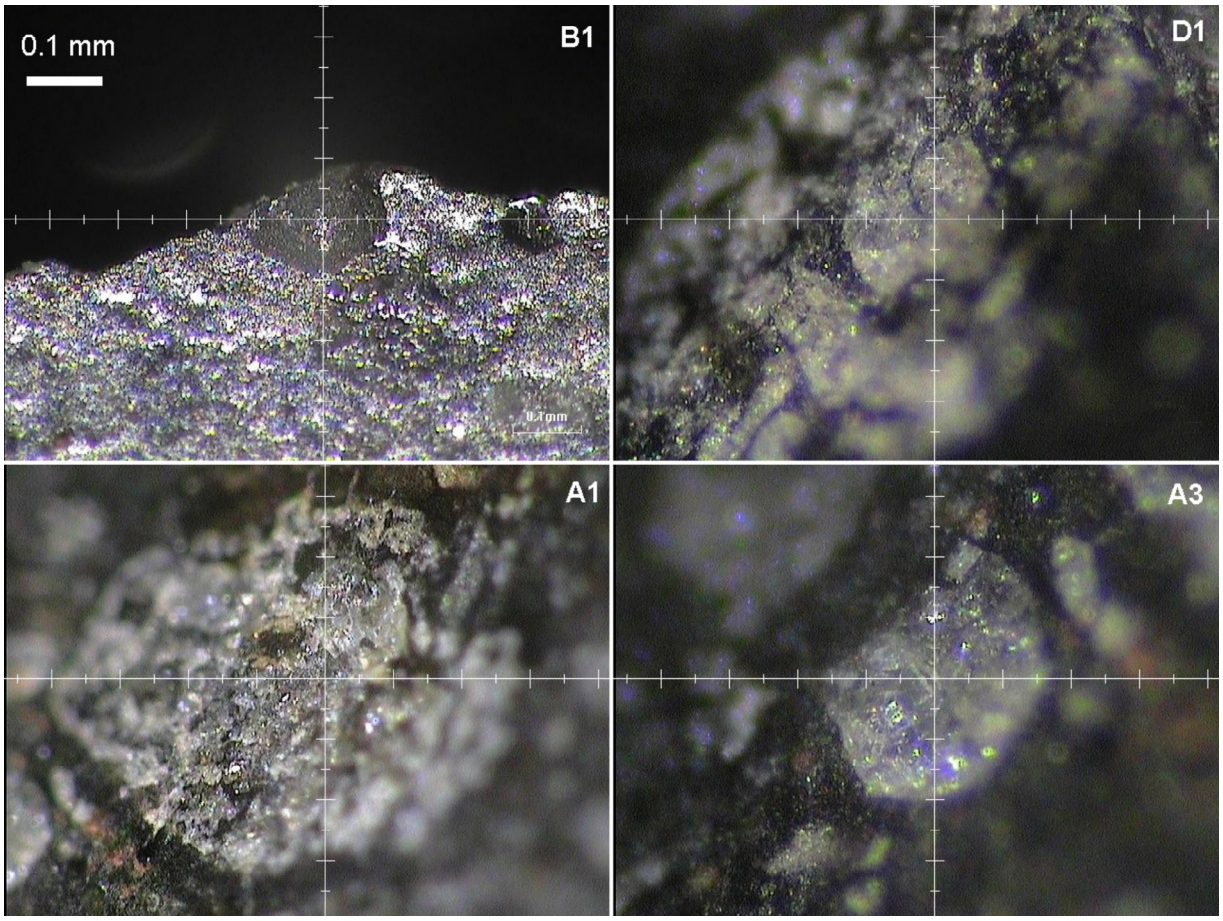

Fig. 1. Field of view images of some measured location (B1, D1, A1, A3). The measuring points are A1, A3 (lower part of sample), B1, C1,D1, R1 (upper part of sample). The olivine has 3 bands for interpretation which are marked by ol11, ol2, ol3.

between incident ray and reflected ray). After exposure, the imaging plate is scanned by a laser-readout system, completing the read process in approximately one minute. The resulting diffraction images were then first processed using the 2DP RIGAKU software, which was used to select the integration area and to do the conversion into a 2θ vs. intensity plot. The final data interpretation from this plot was done in the RIGAKU PDXL 1.8 software.

Mineral phase identification was conducted using Rigaku laboratory software by M. Szabó, focusing on the most characteristic 2θ bands for each mineral. The key peaks were selected as follows:

Olivine: three primary bands at $2\theta = 25°$, $32°$, and $36°$
Orthopyroxene (opx): $2\theta = 28°$
Clinopyroxene (augite, cpx): $2\theta = 43.3°$
Carbonates: calcite at $2\theta = 29$ °, siderite at $2\theta = 42°$
Magnetite: $2\theta = 43.9°$
Spinel: $2\theta = 44.2°$

Additional detail on band positions and mineral associations is available in the Supplementary Online Material SOM1/A-L tables.

The corresponding d-spacing values –defined as the inter-atomic spacing in Angstrom units – were computed from the measured 2θ peak positions, the order of reflection, and the X-ray wavelength using the XRD interpretation software. The full width at half maximum of the peaks (2θ values) are noted as FWHM in the diffractogram.

3. Results

In this section first the MicroXRD results are presented with the details according to different minerals, then VIS–NIR measurements are listed, and later the observed trends are summarized before the 4. Discussion section. The microXRD measurements were done at distinct areas of the sample, which are presented by variation of d values and FWHM of each mineral, listed separately by the mineral types below. The numerical values are given in nm below.

3.1. MicroXRD results

The Fig. 2. shows XRD measurements of the A3 area before and after the irradiations. The lowest intensity

occurs after the 2nd irradiation (grey pattern, spectrum 3106). The d values, FWHM values and the 2θ values are listed in Tables SOM1/C.

The A3 area shows bands with decreasing intensities until the second irradiation (Fig. 2, grey line in the diffractogram). The d and FWHM values are displayed in different tables (Tables SOM1/A-L opx-cpx–ol-mag, carb in SOM) for each mineral. The highest variation before irradiation for adjacent measuring points are displayed by red and bold letters (Tables XRD FWHM and d values opx, cpx, ol, mag, carb in SOM). The FWHM and d values did not show a coherent trend (same changes along with the increasing level of irradiation), only with carbonates can we observe a monotonic increase until the 3rd irradiation in the FWHM and d values.

3.1.1. Key minerals

The orthopyroxene (enstatite), clinopyroxene (augite), and olivine were the major minerals in the sample. Orthopyroxene was identified at 6 locations, clinopyroxene at 3 locations, olivine at 12 locations. Altogether 12 locations were measured before and after each 3 irradiation actions.

Orthopyroxene (enstatite). The orthopyroxene was detected at A (A1, A2, A4, A1 top), B1, and R1 locations.

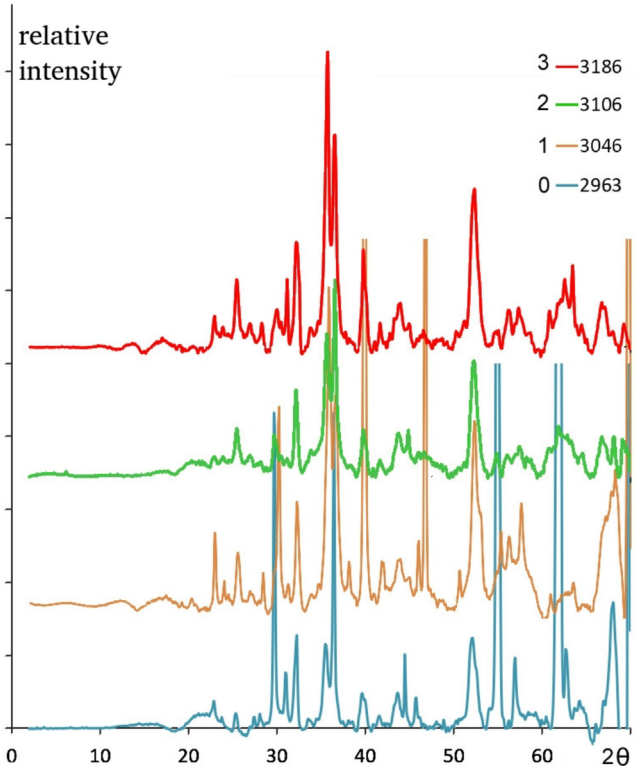

Fig. 2. XRD diffractogram of A3 area, numbers 0–3 mark different irradiation actions, where 0 is for the intact sample. The diffractograms are marked by numbers in each measurement area, where the lowest one is before irradiations, the highest one is after the 3rd irradiation. The four digits number at top right mark the code of the given measurement.

The highest FWHM values were present after the 3rd irradiation. The average values (of different measuring points composed of the same type of mineral) show an increasing trend after each irradiation (Table SOM3/A1a), although the FWHM values for each sample vary after the irradiations; however, the trend in average values is clear. The d value is also increasing, however highest average d value occurred after the 2nd irradiation (Table SOM3/A1a-b) for 2 locations (A1, A2) of 7 measuring points. The highest average FWHM and deviation occur after the 3rd irradiation here, but at different locations show variable trends. However, at d values the highest average and deviation occur after the 2nd irradiation. Only at A1 top location showed both the highest FWHM and the highest d value after the 3rd irradiation.

Clinopyroxene (augite). The clinopyroxene (augite – $(Ca,Na)(Mg,Fe,Al,Ti(SiAl)_2O_6)$) was identified at B1, C1, and D1 locations. In tables XRD cpx the FWHM and d value are listed for the major band at 2.08 nm (d value, Table SOM1/i-k) with variation FWHM values are indicated in Tables of FWHM value (Table SOM3/B1a). The differences of FWHM are the highest after the 1st irradiation, and the biggest difference in spectra FWHM is present after the 1st irradiation. In case of augite, the metastable state after the 1st irradiation indicated by the highest variation and value. The strongest band of clinopyroxene is at d value 2.09, related to the (-233) hkl index of crystalline lattice (Yakovenchuk et al., 2019).

Olivine:. Fo-Fa range (Fo50-Fa50) are characterized by 3 major XRD bands, which are marked by numbers (ol1 (lattice (031), ol2 (lattice (131) ol3) (lattice (211). FWHM values are indicated in Tables SOM1 a-l.

Band ol1 (lattice (031), FWHM): the average d values show a decreasing trend, but the deviation shows an increasing trend until the 3rd irradiation (Table S4a). The highest FWHM values are marked by red letters, presenting trends after the irradiations (Table SOM1/a-l). The highest FWHM values are marked by yellow colour. Numerical results of the measurements can be read in Table SOM1/A-L. Band ol3 ((211) lattice, FWHM) numerical results of the measurements can be read in Table SOM1/A-L.

The results on the variation of d values indicate changes in the mineral crystal structure. The ol1 band (hkl 031) shows decreasing average values (Table SOM3/C2a), suggesting a shortening of the atomic distance at the (031) crystal plane due to the deformation of the crystalline structure. Numerical results for the ol1 band (d value of lattice (031), 2.7A°) are presented in Table SOM3/C2a. Numerical results for the ol2 band (d value of lattice (031), 2.7A°) are provided in Table S4b, and those for the ol3 band (d value of lattice (311), 2.4A°) are listed in Table SOM3/C2c.

3.1.2. Auxillary minerals

Magnetite. was identified at A3, A4, and B2, R1 locations. In A3 it shows decreasing trend in FWHM by the

irradiations, but of A4, R1, B1 locations show variable trends (Table SOM3/D1a). The highest FWHM values occur after the 1st irradiation in case of R1 and A3 areas, whereas in case of A4 after 2nd irradiation, and in case of B1 after 3rd irradiation. But the highest deviation of measuring points and highest maximum of FWHM occur in B1 area after the 3rd irradiation. The highest variations of FWHM occur after the 3rd irradiation (marked by red letters). The highest value in d value occurred after the 2nd irradiation in case of A4 and B1 locations (Table SOM3/D1b). Consistent trend cannot be observed in FWHM values. The average of d values shows a decreasing trend, but the deviations show an increasing trend until the 3rd irradiation (Table SOM3/D1b). The strongest d value of magnetite is near 2.09, which is (400) hkl index of the crystal lattice (Hicks et al., 2017; Noval and Carriazo, 2019), which of variation was analyzed after the irradiation in our sample.

Carbonate. mineral occurs in B1, R1 (calcite – marked by blue cells Table SOM3/E), and in A1 top (siderite - marked by pink cells). The highest d values occurred after the 3rd irradiation both of siderite and calcite (Table SOM1/i, L) for B1, R1 (calcite) and A1 top (siderite) measuring areas (Table SOM3/E1b). Regarding FWHM values the highest average value occur after the 2nd irradiation of carbonates, however no evident trend is visible comparing the different measurement locations (Table SOM3/E1a). The d value near 3.02 corresponds to hkl index (104) (Wang et al., 2019).

3.2. VIS–NIR measurements

The bulk sample of NWA10580 meteorite was measured with near infrared spectroscopic method before and after each irradiation action. These measurements identified pyroxene (735, 1843 nm) and olivine (844, 874 nm) using peak data after Moriarty and Pieters (2016) and Pieters et al. (2008). OH band (1445 nm) also emerged, related band positions with FWHM values are listed in the Table 3.

Comparing the recorded spectra of other works, especially to Cloutis et al. (2012), who surveyed spectral reflectance properties of CO-type carbonaceous chondrites, the following findings are relevant. The spectral feature in the 1 μm region was absent in our sample, however a related silicate peak was evident before the strongest irradiation around 0.8 μm. This later corresponds to local reflectance maximum in several CO meteorites (Cloutis et al., 2012). The 1 μm region feature is attributed to Fe-bearing amorphous phases and also Fe-poor olivine. This has not been emerged in our sample, probably as it was not heavily weathered and shock metamorphized what is required for substantial amount of amorphous phases. We confirm the pyroxene peak around 2 μm that is also abundant in many chondrites (Dunn et al., 2010). Further comparison with two other CO type meteorites (ALH 83108 and ALHA 77003) is shown in Fig. 3, displaying a similar spectral shape and confirming that the sample used in this study is representative.

The irradiation resulted the following modifications of the pyroxene mineral. Please note that the indicated values are averages from several different measurements of the same mineral type. Below we only list exact values, for the uncertainties please refer to Table 1.

- The band around 735 nm shifted with +7 nm after the 1st irradiation and with +4 nm after the 2nd irradiation. After the 1st irradiation the band 730 nm shows 28 nm higher FWHM values. The FWHM values indicate structural deformation: 143 nm at 741 nm after the 2nd irradiation. The FWHM after the 2nd irradiation increased by 45 nm. The band 735 nm disappears after the 3rd irradiation. The pyroxene peak position varies between 741 and 730 nm until the 2nd irradiation, and disappears after the 3rd irradiation.
- The band around 1940 nm shifted with −9 nm after the 1st irradiation, with −3 nm after the 2nd, and + 7 after the 3rd irradiation. After the 1st irradiation the FWHM values were 13 nm less. The FWHM varies between 90 nm and 112 nm during the irradiation process, which could indicate structural deformation. No clear broadening or narrowing could be determined.

Before the irradiation the olivine contains both of major bands at around 847 nm and 863 nm.

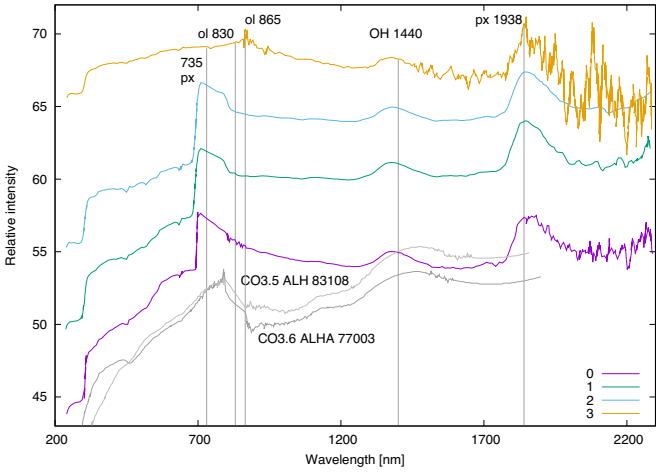

Fig. 3. The VIS–NIR spectra can be seen upward indicating the level of reflectance and numbers indicating the irradiation actions (0: non-irradiated, 1: 1st irradiation, 2: 2nd irradiation, 3: 3rd irradiation). The curves have been vertically offset for clarity. The peak positions with minerals are marked with black text in nm. The pyroxene band at 735 nm disappears after the 3rd irradiation (blue spectrum). For comparison spectra of two other CO chondrites are visualized at the bottom as two gray curves Trigo-Rodríguez et al. (2014).

Table 1
FWHM and band positions (in nm) before and after the irradiations. The band column refers to the peak position. Band and FWHM values were fitted using the Fityk software then manually adjusted. The listed uncertainties were also calculated by Fityk. These findings represent a conservative approach and are suitable for comparing values across different irradiation cycles, as the same determination method was used throughout. Some FWHM and position values had too high errors, these are written in gray color, while peaks that could not be found are denoted with the "-" symbol.

	Pyroxene		Olivine		Olivine		Pyroxene		OH	
Irradiation	band	FWHM	band	FWHM	band	FWHM	band	FWHM	band	FWHM
Before irr.	1948 ± 2	103 ± 4	847 ± 3	10 ± 7	863 ± 3	10 ± 7	730 ± 3	70 ± 9	1447 ± 5	110 ± 11
1st irr.	1937 ± 12	90 ± 12	819 ± 7	70 ± 14	866 ± 4	14 ± 10	737 ± 4	98 ± 12	1445 ± 9	123 ± 16
2nd irr.	1934 ± 3	112 ± 4	825 ± 4	49 ± 11	874 ± 24	43 ± 40	741 ± 2	143 ± 16	1449 ± 2	147 ± 4
3rd irr.	1941 ± 2	94 ± 2	–	–	–	–	–	–	1449 ± 1	134 ± 3

- After the 1st irradiation the band 847 nm shifted to a lower wavelength (to 819 nm). After the 2nd irradiation the band shifted to 825 nm. The FWHM appeared to enlarge in the case of both olivine bands, however the uncertainties were above 20%, so a clear behaviour could not be determined.
- After the 1st irradiation the band 863 nm did not shift outside the error range, and after the 2nd irradiation the error of the position determination was much higher. The band appears to shift gradually to higher wavelengths, however because of the uncertainty, it is possible that the peak remained relatively unchanged. The peak disappeared after the 3rd irradiation.

The spectral slope values of the spectra, normalized to unity at 550 nm and fitted between 200–700 nm, are listed in Table 2. The slope decreased with irradiation with respect to wavelength, meaning that the irradiated spectra is bluer with each step. The region between 700–2300 nm did not exhibit a consistent bluing or reddening.

3.3. Observed trends

Among the wide range of results, some did not exhibit clear trends throughout the irradiation sequence. These cases may warrant further investigation to clarify the underlying mechanisms. In the following sections, we focus on results where distinct irradiation-induced trends were identified and, where applicable, relate them to existing literature. However, in several instances, no directly comparable findings have been reported to date; nonetheless, these new observations may offer valuable insights to the scientific community, even in the absence of obvious trends. The results are organized by mineral type, summarizing observed changes during irradiation, while broader interpretations and comparisons with previous studies are presented in the 4. Discussion section.

3.4. XRD based d values of minerals

Three main minerals (olivine, clinopyroxene, orthopyroxene) and 3 minor minerals (carbonates – siderite and calcite, and magnetite) are presented below.

- The average d values show a decreasing trend in case of *clinopyroxenes* until the 3rd irradiation, but the deviation shows an increase until the 2nd irradiation.
- In case of *orthopyroxene* the average and deviation of d values show an increasing trend until the 2nd irradiation, then show a decrease until the 3rd irradiation.
- The *olivine* has 3 major bands in the XRD diffractogram, which are marked as ol1, ol2, ol3. The averages of d values of olivine (bands ol1, ol2, ol3) show the following trends: decreasing average of d value after the 1st irradiation of the band ol1 (031), no change of average d value can be seen after the 2nd irradiation, then shows a decreasing trend until the 3rd irradiation. Altogether the d value of ol1 (031) decreased roughly until the 3rd irradiation. Variable average trend of d value of the band ol2 (131), and monotonic increasing trend from initial state (before irradiation) until after the 3rd irradiation of the band ol3 (211) could be observed.
- In the case of *magnetite* the highest deviation occurs after the 3rd irradiation, while average d value shows a decreasing trend at the 1st irradiation, then an increase until the 2nd irradiation, and then a decrease until the 3rd irradiation – so no coherent trend could be identified.
- The *carbonates* show monotonic increase of d values until the 3rd irradiation due to amorphization.

3.5. XRD FWHM change of minerals

The average values of *the* FWHM of *clinopyroxene* show increase after the 1st irradiation, then decrease until the 3rd

Table 2
Spectral slope values fitted over the 200 −700 nm region of the spectra. The spectra were normalized to unity at 550 nm.

Irradiation step	0	1	2	3
Slope [%/(10^{3}Å)]	4.41 ± 0.12	3.35 ± 0.11	2.43 ± 0.12	1.03 ± 0.06

irradiation. The deviation of FWHM clinopyroxene shows variable trend, the highest deviation occurs after the 2nd irradiation, so no general trend could be observed.

In case of *olivine*, 3 strong bands were described, where the average FWHM shows decreasing trend (ol1, ol2) for the whole irradiation cycle; and in case of ol3 after the 1st irradiation occurred the highest average value while decreasing happened later. The FWHM deviation of the bands ol1 and ol2 of olivine shows decreasing trend until the 3rd irradiation. The FWHM deviation of the band ol3 of olivine shows an increasing trend only after the 1st irradiation.

No clear trend was observed in the case of *magnetite*, the highest FWHM values occur after the 1st irradiation, but highest deviation occurs after the 3rd irradiation (decreases until the 2nd irradiation, then increases until the 3rd irradiation). The magnetite shows different trends for each measuring point: A4 has the highest value after the 2nd irradiation, and B1 after the 3rd irradiation also increased.

The *carbonates* showed an increasing average FWHM (XRD) trend until the 2nd irradiation. The deviation was the highest after the 1st irradiation, then decreased until the 3rd irradiation. The FWHM depends on the crystallographical orientation, not only by amorphisation effect in XRD patterns, or the crystal lattice defect may be present before the irradiation already. During the irradiation the structure was damaged in all points causing decreasing deviation. In the case of *orthopyroxene*, the deviation and average FWHM show a monotonic trend until the 3rd irradiation in the whole experiment series. Average FWHM increases until the 1st irradiation of clinopyroxene, then shows a monotonic decreasing trend until the 3rd irradiation (with highest deviation after the 2nd irradiation).

3.6. VIS–NIR FWHM change of minerals

The FWHM change does not show a consistent trend at the band around 1938 nm, however it showed an increasing trend of the 735 nm pyroxene band. The position of the 1938 nm band did not change consistently, while the 735 nm band gradually shifted to higher wavelengths. Both olivine bands disappeared after the 3rd irradiation. The 835 nm band seemed to shift to lower wavelengths, while the position of the 860 nm band remained within the error range.

3.7. VIS–NIR change of peak positions of minerals

Pyroxene and olivine showed characteristic modifications of 2–2 bands in the NIR spectra with the following changes during the irradiation:

- *Pyroxene*: Band 1938 nm of pyroxene showed a variable trend throughout the irradiation in terms of position and FWHM change. The 735 nm band gradually shifted to higher wavelengths with an increasing FWHM each irradiation around until it disappeared after the 3rd irradiation.
- *Olivine*: the peak position of band 835 nm showed a decreasing trend until the 2nd irradiation, and disappeared after the 3rd irradiation. The band 860 nm could have possibly shifted to higher wavelengths, and then disappeared after the 3rd irradiation. The FWHM also increased by each irradiation, but the error was over 20%, so this is not a clear trend.
- The *pyroxene* and *olivine* show decreasing MIR peak position at both bands, which indicates Mg loss in structure in olivine and pyroxene (Lantz et al., 2017).

4. Discussion

Among the various changes considering the d and the FWHM values of the irradiation series, only in selected cases could a coherent trend be observed. In the other cases probably metastable modifications happened, or these minerals might have elevated density of lattice faults originally, and further crystalline destruction happened in a stochastic manner, which is supposed by the authors of this work as a relevant possibility. The decrease of d values after the irradiations indicates a shortening of d spacing between atoms in the crystal lattice. The amorphization-induced variation of d values (shortening and elongation) was described by Németh et al. (2022) in case of shocked diamonds, confirming cell size modification. The change of d values in microXRD spectra (decrease of d values ol1 band of olivine, and increase of d value of orthopyroxene and carbonates) indicates Mg loss from the crystal lattice (Huang, 1989; Lee and Lindgren, 2016; Weber et al., 2020). The d-value is related to elemental spacing and not spatial ordering of elements, thus amorphization does not necessarily modify d-value, although it might change in specific cases. The deviation of d values at band ol1 shows an increasing trend until the 3rd irradiation due to amorphization. The band ol2 of olivine deviation shows an increasing trend until the 2nd irradiation, while the deviation of d values of band ol3 shows a decreasing trend until the 3rd irradiation.

Carbonates are more sensitive than silicates to the proton irradiation. The deviation of their d spacing values shows an increasing trend until the 3rd irradiation.

The observed disappearance of the *olivine* major bands after the 3rd irradiations and possibly increasing FWHM values also indicate structural disordering (Gavin et al., 2013), while the shift to a lower wavelength (band 835 nm) indicates an increase of Fe^{2+} in the crystal structure (Hamilton, 2010). The band near 1440 nm corresponds to O–H stretch and deformation, which has less intense, broader bands comparing to regular mineral bands mentioned before. This band has higher intensity than the background, hence the 1440 nm moisture band belongs to the sample. The OH band may be originated by terrestrial weathering. The OH band does not show considerable position shift throughout the irradiations, while the FWHM appears to gradually increase. However, influence

by the environmental humidity on adsorbed water content could not be excluded. The NIR is more sensitive to changes in the crystal lattice related to the amorphization, and the disappearance of major band 860 nm can be observed in the case of olivine.

In the case of *orthopyroxene*, the increase of d and FWHM values after every irradiation indicate a stretching (elongation) of the crystal lattice, caused by Mg loss. This feature was described by Brunetto et al. (2006, 2015, 2017) regarding their TEM and IR measurements. The average FWHM values of orthopyroxene show monotonic increase after the irradiation actions. The highest average FWHM values of orthopyroxenes after the 3rd irradiation indicate that the orthopyroxene is more sensitive for increasing fluence and time of irradiation, than the clinopyroxene. The increasing FWHM indicates irradiation related disordering of crystal structure due to incorporation of H^+ ions. An increasing trend of FWHM and disappearance of band after the 3rd irradiation of olivine were also observed. These changes may have occurred by incorporation of H^+ ions.

After the 3rd irradiation, the FWHM values of *magnetite* indicate the biggest change in crystal lattice. The *feldspar* was sensitive for irradiation, as it disappeared after the 2nd irradiation in Raman spectra, and disappeared after the 3rd irradiation in FTIR spectroscopy. *Spinel* showed an increasing trend in peak shift in FTIR spectroscopy, but in XRD showed a variable trend, because of variation of distance of atoms in the crystal lattice.

4.1. Comparison with previous works

Several observations of this work present unique reference data, which have not been provided before. Only olivine has been studied in the published references after irradiation (Yang et al., 2016) by XRD method, where the band ol1 shows similar trend to their work regarding FWHM. Olivine (Yang et al., 2016) and feldspar (Kayama et al., 2011b; Kayama et al., 2011a) after irradiation were studied previously, which trends can be extrapolated to other minerals, like spinel and pyroxene. The variation of FWHM of XRD bands of olivine and pyroxene is documented only in our work after irradiations, however Kayama et al. (2012) found a slight increase of FWHM of XRD bands of shocked feldspars. Shimadzu (NIR) measurements were done only in our study for specific targets after proton irradiation. The variation of d values of pyroxene were only documented in our work.

Yang et al. (2016) studied olivines after 5 irradiations (5 mJ/pulse), but they could not observe any position change of all main diffraction peaks determined by the atomic distance within the mineral structure of olivine. Our olivine analysis shows changes in d values after all irradiations in case of 3 major bands (ol1-ol3). Irradiated olivine by flux 1×10^{17} ions/cm^{-2} on 50 keV. He^+ which has been injected to the oriented olivine crystals along the [010] axis and vertically impacts the MO6 octahedra chains in the experiment of Yang et al. (2016). Only part of the crystal planes parallel to the MO6 octahedra chains, such as (040), is destroyed seriously (Yang et al., 2016). Most of the MO6 octahedra chains and SiO_4 tetrahedra have been completely saved. SiO_4 tetrahedra and MO6 octahedra have been substituted by He^+ or knocked out to form lattice defects or interstitial atoms (Yang et al., 2016). The band ol3 (211) shows monotonic increase of d values indicating an increase of atomic space in the crystal lattice due to Mg loss, which has been identified using TEM by Brunetto et al. (2006) and Lantz et al. (2017).

Yang et al. (2016) observed amorphization-related d spacing at 2.5 ((131) plane) value and at 2.8 ((041) plane) and decreasing of d values after the irradiation. In our case, decreasing of d spacing in median value of olivine is the highest after the 3rd irradiation with a similar flux to that used by Li et al. (2013), who observed a decrease in d values, indicating amorphization. Higher fluxes of irradiation can damage the SiO_4 tetrahedra substantially, after distortion of the MgO_6 octahedra (Li et al., 2013). In our data, the decrease of d values in 131 (band ol2) until the 3rd irradiation of olivine indicates shortening of atomic spacing in the crystal lattice, inducing lattice defect. The band ol1 (031) shows decrease in d values until the 3rd irradiation, indicating shortening of atomic distance in crystal lattice due to lattice defect from Mg loss.

The increase of d values indicates Mg loss in the crystal structure in case of olivine and pyroxenes, due to the difference in the size of Fe and Mg cations occupying the crystal lattice. According to Sakuntala et al. (1998), the disordering of crystals is driven by amorphization. This feature can be observed in our XRD diffractograms (Fig. 2. XRD and Table SOM2/A-L patterns) after the 3rd irradiations by variation of intensity and disappearance of minor bands. Németh et al. (2022) observed both increase and decrease of d values in shock-deformed diamonds and concluded that these variations correspond to atomic distance changes in the crystal lattice. The variable trend in d values was observed in ol2-ol1 bands of olivine and at clinopyroxene too. The lack of consistent trends in d values remains unexplored in the literature; however, a similar situation was reported for sulphates by Sakuntala et al. (1998), attributed to orientational disorder and amorphization. The variation of d values due to deformation is well documented for olivine (Yang et al., 2016; Li et al., 2013), carbonate (Németh et al., 2018; Németh, 2021), and feldspar. However, variation of d values of pyroxene and magnetite has not been documented in other works. The trends of d values regarding olivine and pyroxene in our work are similar to Yang et al. (2016, 2013). The irradiation-related changes in XRD and in NIR ranges are also published for the first time in our work.

The variation of the FWHM of studied minerals (olivine, pyroxene, magnetite, carbonates, spinel) was not analyzed in other works, but the amorphization-related

changes in case of our irradiated orthopyroxenes and carbonates (increase of FWHM) are very similar to the shocked feldspar, as described by Kayama et al. (2012). Following Kayama et al. (2012), increasing amorphization is indicated by increasing FWHM values of XRD bands. Earlier tests of artificial He^+ ion bombardment induced structural defects in the crystal lattice, leading to broadening of Raman bands, as observed by (Nasdala et al., 2010). The increase of FWHM by shock deformation in shocked chondrites (olivine, pyroxene) was observed by Rupert et al. (2020) by 1.4° in the case of olivine, and 0.3° in the case of pyroxene, 2θ values in diffractograms. The Raman spectroscopy is more sensitive for irradiation-related changes than FTIR spectroscopy, in the case of major SiO_4 vibrations. 346 Minor bands (bonds Fe/Mg-SiO_4, Fe) show moderately positive peak shifts or disappear when using FTIR and Raman methods. The Fe/Mg–Si bonds are very sensitive to irradiation using both methods. FTIR and Raman data show different trends in case of all minerals. The major bands of olivine and pyroxene show decreasing trends in case of FTIR, but increasing trends in case of Raman spectroscopy.

Although NIR spectra of asteroids and meteorites have been widely investigated, NIR measurement based modifications by irradiation experiments conducted by other researchers have not been extensively studied (except peak data obtained by Moriarty and Pieters (2016) and Pieters et al. (2008)). Only a limited number of studies have performed irradiation experiments followed by NIR spectroscopy (e.g., Loeffler et al. (2009, 2021, 2023)), hence the trends of peak shifts were compared with references from other IR methods (Brunetto et al., 2006; Lantz et al., 2017). While the NIR experiments using irradiations were documented only in our work, changes in MIR (FTIR) measurements have already been well documented by Brunetto et al. (2006, 2015, 2017). They observed negative peak shift due to Mg loss, and disappearance of minor bands due to irradiation, which can be well linked to NIR data.

4.2. Summary of observed changes

Several irradiation related changes were found in the sample, however evident trends could be identified only in some cases. Example NIR spectra of the sample after the 2nd irradiation can be seen in Fig. 4. at the top, while trends of FWHM changes are presented below, visualizing the broadening of infrared peaks caused by the irradiation.

The following trends could be identified based on Table 3:

- Olivine FWHM shows increasing trend in Raman, NIR, and ol1 band in XRD, but shows decreasing trend in case of MIR. The increasing FWHM is caused by amorphisation due to the irradiations (Kayama et al., 2012), which can be better observed at Si-Fe/Mg bonds than in case of SiO_4 tetrahedra. Using XRD data, the FWHM is influenced not only by amorphisation, but by orientation of measured minerals too.
- The pyroxene is more sensitive to irradiation-induced amorphisation than olivine or spinel, because it shows increasing trend in FWHM for XRD, NIR, Raman, and MIR data. Increasing trend in FWHM due to irradiation was observed by Gucsik et al. (2020), but decreasing of FWHM in MIR was not yet described by others.
- The carbonates are very sensitive to irradiation, based on our observations. The Fe/Ca/Mg bonds are less stable than the Fe-O bonds in magnetite. Considering minor components, calcite FWHM shows increasing trend with Raman and XRD. Magnetite shows a straightforward but variable trend in FWHM change with Raman and XRD. Calcite and siderite show increasing trends in case of Raman shift and XRD d values. The carbonates show continuous increase in d value until the 3rd irradiation.

4.3. Astrophysical relevance

It is worth considering whether such spectral changes caused by the weathering process could be identified in the future by asteroid missions. At the beginning of the process, with weaker irradiation levels, somewhat stochastic changes are present without a strong trend. This is related to the inferred metastable-like changes, which partly distort the crystalline lattice to a limited extent. Although the changes are moderately small, such modifications might emerge at the beginning of the space weathering process – for example, when material becomes exposed on asteroid surfaces, such as by sudden mass wasting or fresh impact excavation. While collisional gardening acts across all spatial scales, most meteoroids impacting airless bodies are micron to cm-sized projectiles, producing breccias, depleting volatiles, and implantating projectile materials. These processes alter the mechanical properties of the regolith, as measured in particles from asteroid Itokawa Tanbakouei et al. (2019), further influencing surface evolution.

The results presented here are valuable for comparison to the artificial weathering tests of olivine and pyroxene samples using He and Ar ions (Chrbolková et al., 2021) with laser shots. These experiments demonstrated that spectral slope changes are consistent with observations of A-type asteroids, while the lack of significant slope changes in pyroxene are consistent with asteroid (4) Vesta. These findings suggest that it might be possible to distinguish the products of these two agents of space weathered surface using NIR range; however, in the MIR range, the situation appears more complex, as shown in this study.

It should be considered during high spatial resolution infrared analysis of fresh craters, as it might make the iden-

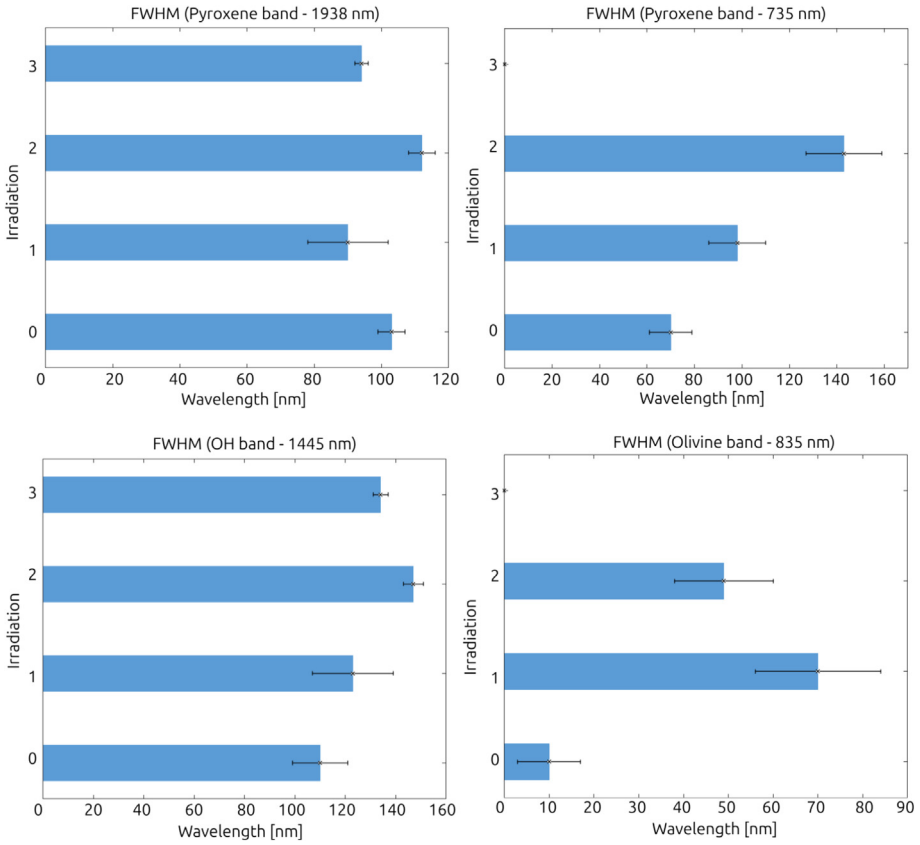

Fig. 4. Trends of FWHM change for bands (for data see Table 1.). The uncertainties for the olivine band around 860 nm was too high so it is not represented here. If the band disappeared upon irradiation, the bar is missing. from the graph.

tification of specific minerals (like subtypes of pyroxenes or olivines) uncertain. There are CubeSat-based missions equipped with high resolution VIS–NIR spectrometers, specifically designed to detect such surface changes and compositional variations caused by irradiation and impact processes, offering a promising way for detecting early signs of space weathering (Kohout et al., 2018). It is also worth considering that such observations might offer further insight into regolith mixing and fragmentation, as well as possible asteroid size related regolith processing aspects, such as the locations and areal ratio of exposed and poorly weathered material (Beitz et al., 2016), which could be better understood through continued study.

In case of more intense irradiation and extended-duration space weathering, there is a general trend toward amorphization, leading to more observable spectral changes. Focusing on the specific bands indicated in Fig. 3. (especially 1938 nm for pyroxene and 820 nm for olivine), these could be used to roughly estimate the level of weathering and the related scale of exposure duration. To evaluate such aspects for upcoming missions, comparative measurements of the same specific mineral bands at different areas of the asteroids should be in the focus. With improved infrared detectors, band depth comparison could highlight more and less space-weathered areas, opening the possibility to estimate the relative duration of exposure for various locations, and further indicating temporal differences in surface modifications.

5. Conclusion

In this study, microXRD and NIR measurements were performed on NWA 10580 meteorite, and compared to Raman and FTIR measurements before and after controlled artificial proton beam-induced modifications. Changes were realized by H^+ irradiation simulating solar wind protons, administered at three stages with 1 keV voltage as follows: 15 s (10^{11} ion/cm^2) for the 1st irradiation, for 1 h (10^{14} ion/cm^2) for the 2nd irradiation, and for 1 day (10^{17} ion/cm^2) for the 3rd irradiation.

The spectral slope exhibited clear bluing upon irradiation in the 200–700 nm range, while there was no clear reddening or bluing between 700–2300 nm. Bluing with irradiation has been reported for space weathered carbonaceous materials, for example in the works of Clark et al. (2011); Matsuoka et al. (2015); Matsuoka et al. (2020). Cloutis et al. (2011) showed that opaque-phyllosilicate mixtures lower overall reflectance, with spectral slopes reddening or bluing depending on opaque type and abundance, and bluing specifically linked to magnetite and graphite.

Table 3
Summary table showing changes of peak positions (MIR, NIR, Raman), and XRD d values with FWHM modifications. The trends in XRD and Shimadzu are written in text detail, which are compared trends in Raman and FTIR. Where consistent trends are observed until the 3rd irradiation, are mentioned as increasing/decreasing in the cells. Where there are no trends, the cells are marked as variable. Where the trend can be observed until the 2nd irradiation, are marked as decreasing/increasing trend until the second irradiation.

		FTIR MIR (band nm)	Raman (band nm)	NIR, Shimadzu (band nm)	XRD
Olivine	FWHM	decreasing trend for bands 830, 860, disappearance of minor bands	increasing trend for bands 820, 850, disappearance of minor bands	835: increasing 860: disappear after the 1st irradiation, then increase after 3rd irradiation	ol 1 decreasing ol2 - 3 variable
	Peak, d value	bands 830, 860: decreasing, after the 3rd irradiation disappearance of minor bands	bands 820, 850: increasing, after the 3rd irradiation disappearance of minor bands	835: increasing 860: disappear after the 1st irradiation, then increase after the 3rd irradiation	ol1 decreasing ol 2 - ol 3 variable
Ortho-pyroxene	FWHM	decreasing trend for band 1046, disappearance/increasing FWHM of minor bands	increasing trend for band 1008, disappearance of minor bands	735: increasing 1938: increasing until the 2nd irradiation	increasing
	Peak, d value	band 1046: decreasing, after the 3rd irradiation disappearance of minor bands, moderate peak shifts	band 1007: increasing, disappearance of minor band	1938: variable 735: variable	increasing until the 2nd irradiation
Clino-pyroxene	FWHM	–	–	–	variable
	Peak, d value	–	–	–	variable
Calcite	FWHM	–	increasing	–	increasing until 2nd irradiation
	Peak, d value	–	increasing	–	increasing
Siderite	FWHM	–	increasing	–	variable
	Peak, d value	–	increasing	–	increasing
Magnetite	FWHM	–	variable	–	variable
	Peak, d value	–	variable	–	variable
Spinel	FWHM	variable background	high fluorescence –	decreasing	
	Peak, d value	increasing after 2nd and 3rd irradiation background	high fluorescence –	variable	
Feldspar	FWHM	band 1150: increasing FWHM	decreasing until 2nd irradiation, then disappear	–	–
	Peak, d value	variable	increasing, then disappear	–	–

The most evident amorphization occurred by the 3rd irradiation as expected, which was also well-detected in our previous FTIR studies (Gyollai et al., 2024). The XRD data presented here shows variable trends in d values related to the modified spacing distances in the crystalline structure. Only orthopyroxene and carbonates showed continuously increasing trend of d values the 3rd irradiation. This observation aligns with prior findings (Németh et al., 2022), which report atomic distance variations in the crystal lattice due to deformation by shock effects. We demonstrate that irradiation could produce partly shock effect-like distortions.

The decreasing trend of olivine we observed in the ol1 band (XRD d value (031) 2.76A°), due to Mg loss confirmed the earler findings of (Brunetto et al., 2020), and Yang et al. (2016). The FWHM of XRD data has not been extensively studied by other authors; however, Kayama et al. (2011b,a) reported an increase in FWHM for space-weathered feldspars due to irradiation, a trend we also observed for carbonates and clinopyroxenes. Magnetite

showed a decreasing trend in the average d values, although the deviation increases up to the 3rd irradiation. Since FWHM depends on both background and crystal orientation in the diffractogram, it shows variable trends across the studied minerals. Orthopyroxenes and carbonates however exhibit an increasing trend in FWHM. Orthopyroxene exhibits greater sensitivity to increasing fluence and irradiation time than clinopyroxene, as indicated by its higher average FWHM values after the third irradiation. The difference might be related to different bond energies, or also to differences in the occurrences of crystalline lattice deflect or vacancies.

NIR measurements of pyroxene showed an increasing peak position for the major band (1938 nm), while the minor band (735 nm) disappeared after the 3rd irradiation. Olivine displayed a variable trend; however, the 835 nm band increased after the 3rd irradiation, and the other major band 860 nm disappeared after the 1st irradiation. The NIR FWHM showed an increasing trend up to the 3rd irradiation for both olivine and pyroxene. This study provides the first NIR measurements of this kind, which have not been evaluated in other irradiation studies, though similar increasing trends in FTIR studies may used as a comparison (Lantz et al., 2015; Lantz et al., 2017; Brunetto et al., 2018). The observed wide range of modifications offers valuable opportunities for further analysis to enhance our understanding and refine our conclusions.

Based on the recorded spectra, metastable early alteration by space weathering could produce stochastic band changes, what might be identified by well adjusted infrared detectors in the future at fresh slumps and recently excavated craters on asteroid surfaces. For the evaluation of stronger space weathering state, the 1938 nm band for pyroxene and 820 nm band for olivine could be used. Next asteroid sampling missions might provide such exposure data that linked to the weakening of the above indicated two bands could help to roughly estimate the level of weathering and the related scale of exposure duration in the future.

Declaration of competing interest

The authors declare that they have no known competing financial interests or personal relationships that could have appeared to influence the work reported in this paper.

Acknowledgements

This project was supported by the K_138594 project of NKFIH. Z.J. is grateful for the support of the Hungarian Academy of Sciences through the János Bolyai Research Scholarship. The authors also acknowledge the support from the Europlanet 2024 RI which has been funded by the European Union's Horizon 2020 Research Innovation Programme under grant agreement No. 871149.

Appendix A. Supplementary data

Supplementary data associated with this article can be found, in the online version, athttps://doi.org/10.1016/j.asr.2025.11.086.

References

Abe, M., Takagi, Y., Kitazato, K., et al., 2006. Near-infrared spectral results of asteroid Itokawa from the Hayabusa spacecraft. Science 312 (5778), 1334–1338. https://doi.org/10.1126/science.1125718.

Baratta, G.A., Brunetto, R., Fulvio, D., et al., 2010. In-situ studies of ion irradiated materials relevant to planetary science. In: European Planetary Science Congress 2010, p. 249, https://ui.adsabs.harvard.edu/abs/2010epsc.conf..249B.

Beitz, E., Blum, J., Parisi, M.G., et al., 2016. The collisional evolution of undifferentiated asteroids and the formation of chondritic meteoroids. ApJ 824 (1), 12. https://doi.org/10.3847/0004-637X/824/1/12, arXiv:1604.02340.

Bell, J.F., 1988. A probable asteroidal parent body for the CO or CV chondrites. Meteoritics 23, 256–257.

Biri, S., Rácz, R., Pálinkás, J., 2012. Status and special features of the atomki ECR ion sources). Rev. Scient. Instrum., 83(2), 02A341. https://ui.adsabs.harvard.edu/abs/2012RScI...83bA341B. doi:10.1063/1.3673006.

Bonal, L., Brunetto, R., Beck, P. et al., 2015. Visible-IR and Raman microspectroscopic investigation of three Itokawa particles collected by Hayabusa: Mineralogy and degree of space weathering based on nondestructive analyses. Meteorit. Planet. Sci., 50(9), 1562–1576. https://ui.adsabs.harvard.edu/abs/2015M&PS...50.1562B. doi:10.1111/maps.12496.

Brunetto, R., Lantz, C., Dionnet, Z. et al., 2018. Hyperspectral FTIR imaging of irradiated carbonaceous meteorites. Planet. Space Sci., 158, 38–45.https://www.sciencedirect.com/science/article/pii/S0032063317304051. doi:10.1016/j.pss.2018.05.008.

Brunetto, R., Lantz, C., Ledu, D. et al. (2014). Ion irradiation of Allende meteorite probed by visible, IR, and Raman spectroscopies. Icarus, 237, 278–292.https://ui.adsabs.harvard.edu/abs/2014Icar.237.278B. doi:10.1016/j.icarus.2014.04.047.

Brunetto, R., Lantz, C., Nakamura, T., et al., 2020. Characterizing irradiated surfaces using IR spectroscopy. Icarus 345, 113722. https://doi.org/10.1016/j.icarus.2020.113722.

Brunetto, R., Loeffler, M.J., Nesvorný, D. et al., 2015. Asteroid surface alteration by space weathering processes. In: P. Michel, F.E. DeMeo, & W.F. Bottke (Eds.), Asteroids IV (pp. 597–616). https://ui.adsabs.harvard.edu/abs/2015aste.book.597B. doi:10.2458/azu_uapress_9780816532131-ch031.

Brunetto, R., Vernazza, P., Marchi, S. et al., 2006. Modeling asteroid surfaces from observations and irradiation experiments: The case of 832 Karin. Icarus, 184(2), 327–337.https://ui.adsabs.harvard.edu/abs/2006Icar.184.327B. doi:10.1016/j.icarus.2006.05.019.

Burbine, T.H., Binzel, R.P., Bus, S.J., et al., 2001. K asteroids and CO3/CV3 chondrites. Meteorit. Planet. Sci. 36 (2), 245–253. https://doi.org/10.1111/j.1945-5100.2001.tb01869.x.

Chapman, C.R., 2004. Space weathering of asteroid surfaces. Annu. Rev. Earth Planet. Sci., 32, 539–567.https://ui.adsabs.harvard.edu/abs/2004AREPS.32.539C. doi:10.1146/annurev.earth.32.101802.120453.

Chaves, L.C., Thompson, M.S., Dukes, C.A., et al., 2023. Evaluating the effects of space weathering on asteroidal accessory phases: magnetite and pentlandite. In: In 54th Lunar and Planetary Science Conference (p. 1804). volume 2806 of LPI Contributions.

Chrbolková, K., Brunetto, R., Ďurech, J., et al., 2021. Comparison of space weathering spectral changes induced by solar wind and micrometeoroid impacts using ion- and femtosecond-laser-irradiated olivine and pyroxene. A&A 654, A143. https://doi.org/10.1051/0004-6361/202140372, arXiv:2108.00870.

Clark, B.E., Binzel, R.P., Howell, E.S. et al., 2011. Asteroid (101955) 1999 RQ36: Spectroscopy from 0.4 to 2.4 μm and meteorite analogs. Icarus, 216(2), 462–475. doi:10.1016/j.icarus.2011.08.021.

Clark, B.E., Ockert-Bell, M.E., Cloutis, E.A., et al., 2009. Spectroscopy of K-complex asteroids: parent bodies of carbonaceous meteorites? Icarus 202 (1), 119–133. https://doi.org/10.1016/j.icarus.2009.02.027.

Cloutis, E.A., Hiroi, T., Gaffey, M.J., et al., 2011. Spectral reflectance properties of carbonaceous chondrites: 1. CI chondrites. Icarus 212 (1), 180–209. https://doi.org/10.1016/j.icarus.2010.12.009.

Cloutis, E.A., Hudon, P., Hiroi, T. et al., 2012. Spectral reflectance properties of carbonaceous chondrites: 8. "other" carbonaceous chondrites: CH, ungrouped, polymict, xenolithic inclusions, and R chondrites. Icarus, 221(2), 984–1001.https://ui.adsabs.harvard.edu/abs/2012Icar.221.984C. doi:10.1016/j.icarus.2012.10.008.

de León, J., Licandro, J., Duffard, R., et al., 2006. Spectral analysis and mineralogical characterization of 11 olivine–pyroxene rich NEAs. Adv. Space Res. 37 (1), 178–183. https://doi.org/10.1016/j.asr.2005.05.074.

Delbo, M., Libourel, G., Wilkerson, J., et al., 2014. Thermal fatigue as the origin of regolith on small asteroids. Nature 508 (7495), 233–236. https://doi.org/10.1038/nature13153.

DeMeo, F.E., Alexander, C.M.O., Walsh, K.J. et al., 2015. The Compositional Structure of the Asteroid Belt. In: P. Michel, F.E. DeMeo, & W.F. Bottke (Eds.), Asteroids IV (pp. 13–41). doi:10.2458/azu_uapress_9780816532131-ch002.

Dirri, F., Palomba, E., Galiano, A. et al., 2022. VIS-NIR reflectance analysis of (162173) Ryugu analogues mixtures and CC meteorites in the framework of Hayabusa2 mission. In: European Planetary Science Congress (pp. EPSC2022–154).https://ui.adsabs.harvard.edu/abs/2022EPSC...16.154D. doi:10.5194/epsc2022-154.

Dunn, T.L., McCoy, T.J., Sunshine, J.M., et al., 2010. A coordinated spectral, mineralogical, and compositional study of ordinary chondrites. Icarus 208 (2), 789–797. https://doi.org/10.1016/j.icarus.2010.02.016.

Fazio, A., Matthäus, G., Harries, D. et al., 2017. Reproducing space weathering of olivine by using high-energy femtosecond laser pulses. In: A. Heisterkamp, P.R. Herman, M. Meunier, & R. Osellame (Eds.), Society of Photo-Optical Instrumentation Engineers (SPIE) Conference Series (p. 100941D). volume 10094 of Society of Photo-Optical Instrumentation Engineers (SPIE) Conference Series.https://ui.adsabs.harvard.edu/abs/2017SPIE10094E.1DF. doi:10.1117/12.2252130.

Fischer, E.M., Pieters, C.M., 1994. Remote determination of exposure degree and iron concentration of lunar soils using VIS-NIR spectroscopic methods. Icarus 111 (2), 475–488. https://doi.org/10.1006/icar.1994.1158.

Fulvio, D., Perna, D., Ieva, S. et al., 2016. Spectral characterization of V-type asteroids - i. space weathering effects and implications for V-type NEAs. MNRAS, 455(1), 584–595.https://ui.adsabs.harvard.edu/abs/2016MNRAS.455.584F. doi:10.1093/mnras/stv2300.

Gavin, P., Chevrier, V., Ninagawa, K., et al., 2013. Experimental investigation into the effects of meteoritic impacts on the spectral properties of phyllosilicates on Mars. J. Geophys. Res. (Planets) 118 (1), 65–80. https://doi.org/10.1029/2012JE004185.

Gloeckler, G., 2003. Ubiquitous suprathermal tails on the solar wind and pickup ion distributions. In M. Velli, R. Bruno, F. Malara, & B. Bucci (Eds.), Solar Wind Ten (pp. 583–588). AIP volume 679 of American Institute of Physics Conference Series.https://ui.adsabs.harvard.edu/abs/2003AIPC.679.583G. doi:10.1063/1.1618663.

Greenwood, R.C., Burbine, T.H., Franchi, I.A., 2020. Linking asteroids and meteorites to the primordial planetesimal population. Geochim. Cosmochim. Acta 277, 377–406. https://doi.org/10.1016/j.gca.2020.02.004.

Gucsik, A., Futó, P., Simonia, I. et al., 2020. Space weathering-related evolution of fine-grained asteroidal and cometary materials: An implication for sample return planetary missions. EasycChair Preprint 3383.

Gyollai, I., Biri, S., Juhász, Z. et al., 2024. Raman-infrared spectral correlation of an artificially space-weathered carbonaceous chondrite meteorite. Minerals, 14(3), 288.https://ui.adsabs.harvard.edu/abs/2024Mine...14.288G. doi:10.3390/min14030288.

Hamilton, V.E., 2010. Thermal infrared (vibrational) spectroscopy of Mg-Fe olivines: a review and applications to determining the composition of planetary surfaces. Chemie der Erde/Geochem. 70 (1), 7–33. https://doi.org/10.1016/j.chemer.2009.12.005.

Hapke, B., 2001. Space weathering from Mercury to the asteroid belt. J. Geophys. Res., 106(E5), 10039–10074.https://ui.adsabs.harvard.edu/abs/2001JGR...10610039H. doi:10.1029/2000JE001338.

Helfenstein, P., Veverka, J., Thomas, P.C., et al., 1996. Galileo photometry of asteroid 243 Ida. Icarus 120 (1), 48–65. https://doi.org/10.1006/icar.1996.0036.

Helfenstein, P., Veverka, J., Thomas, P.C., et al., 1994. Galileo Photometry of Asteroid 951 Gaspra. Icarus 107 (1), 37–60. https://doi.org/10.1006/icar.1994.1005.

Hicks, L.J., MacArthur, J.L., Bridges, J.C. et al., 2017. Magnetite in comet Wild 2: Evidence for parent body aqueous alteration. Meteorit. Planet. Sci., 52(10), 2075–2096.https://ui.adsabs.harvard.edu/abs/2017M&PS...52.2075H. doi:10.1111/maps.12909.

Huang, P., 1989. Feldspars, olivines, pyroxenes, and amphiboles. In Minerals in Soil Environments chapter 20. (pp. 975–1050). John Wiley & Sons, Ltd.https://acsess.onlinelibrary.wiley.com/doi/abs/10.2136/sssabookser1.2ed.c20. doi: 10.2136/sssabookser1.2ed.c20. arXiv: https://acsess.onlinelibrary.wiley.com/doi/pdf/10.2136/sssabookser1.2ed.c20.

Jakubek, R.S., Fries, M.D., 2022. Calibration of the temporal drift in absolute and relative Raman intensities in large Raman images using a mercury-argon lamp. J. Raman Spectrosc., 53(1), 137–147.https://ui.adsabs.harvard.edu/abs/2022JRSp...53.137J. doi:10.1002/jrs.6259.

Kanuchova, Z., Brunetto, R., Fulvio, D. et al., 2015. Near-ultraviolet bluing after space weathering of silicates and meteorites. Icarus, 258, 289–296.https://ui.adsabs.harvard.edu/abs/2015Icar.258.289K. doi:10.1016/j.icarus.2015.06.030.

Kayama, M., Nishido, H., Sekine, T. et al., 2012. Shock barometer using cathodoluminescence of alkali feldspar. J. Geophys. Res. (Planets), 117 (E9), E09004. URL:https://ui.adsabs.harvard.edu/abs/2012JGRE.117.9004K. doi:10.1029/2011JE004025.

Kayama, M., Nishido, H., Toyoda, S. et al., 2011a. Combined cathodoluminescence and micro-raman study of helium-ion-implanted albite. Spectrosc. Lett., 44(7–8), 526–529.https://ui.adsabs.harvard.edu/abs/2011SpecL.44.526K. doi:10.1080/00387010.2011.610415.

Kayama, M., Nishido, H., Toyoda, S. et al., 2011b. Radiation effects on cathodoluminescence of albite. Am. Mineral., 96(8–9), 1238–1247. https://ui.adsabs.harvard.edu/abs/2011AmMin. 96.1238K. doi:10.2138/am.2011.3780.

Keller, L.P., McKay, D.S., 1993. Discovery of vapor deposits in the lunar regolith. Science, 261(5126), 1305–1307. https://ui.adsabs.harvard.edu/abs/1993Sci...261.1305K. doi:10.1126/science.261.5126.1305.

Kitazato, K., Milliken, R.E., Iwata, T., et al., 2019. The surface composition of asteroid 162173 Ryugu from Hayabusa2 near-infrared spectroscopy. Science 364 (6437), 272–275. https://doi.org/10.1126/science.aav7432.

Kohout, T., Näsilä, A., Tikka, T., et al., 2018. Feasibility of asteroid exploration using CubeSats—ASPECT case study. Adv. Space Res. 62 (8), 2239–2244. https://doi.org/10.1016/j.asr.2017.07.036.

Kovács, I., Németh, T., Kiss, G.B. et al., 2021. Application of the capillary method in micro X-ray diffractometry (μ-xrd): A useful technique for the characterization of small amounts of clay minerals. Central European Journal of Geology, 64(1), 1–7. URL: https://ui.adsabs.harvard.edu/abs/2021CEJGl.64....1K. doi:10.1556/24.2020.00005.

Lantz, C., Brunetto, R., Barucci, M.A., et al., 2015. Ion irradiation of the Murchison meteorite: visible to mid-infrared spectroscopic results. Astron. Astrophys. 577, A41. https://doi.org/10.1051/0004-6361/201425398.

Lantz, C., Brunetto, R., Barucci, M.A. et al., 2017. Ion irradiation of carbonaceous chondrites: A new view of space weathering on primitive asteroids. Icarus, 285, 43–57. URL: https://ui.adsabs.harvard.edu/abs/2017Icar. 285...43L. doi:10.1016/j.icarus.2016.12.019.

Lee, M.R., Lindgren, P., 2016. Aqueous alteration of chondrules from the Murchison CM carbonaceous chondrite: Replacement, pore filling, and the genesis of polyhedral serpentine. Meteorit. Planet. Sci. 51 (6), 1003–1021. https://doi.org/10.1111/maps.12644.

Li, Y., Li, X., Wang, S. et al., 2013. Crystal orientation results in different amorphization of olivine during solar wind implantation. J. Geophys. Res. (Planets), 118(10), 1974–1982. URL: https://ui.adsabs.harvard.edu/abs/2013JGRE.118.1974L. doi:10.1002/jgre.20151.

Loeffler, M.J., Dukes, C.A., Baragiola, R.A., 2009. Irradiation of olivine by 4 keV He^{+}: simulation of space weathering by the solar wind. J. Geophys. Res. (Planets) 114 (E3), E03003. https://doi.org/10.1029/2008JE003249.

Lucey, P.G., Blewett, D.T., Taylor, G.J., et al., 2000. Imaging of lunar surface maturity. J. Geophys. Res.: Planets 105 (E8), 20377–20386. https://doi.org/10.1029/1999je001110.

Mahlke, M., Eschrig, J., Carry, B., et al., 2023. Spectral analogues of Barbarian asteroids among CO and CV chondrites. A&A 676, A94. https://doi.org/10.1051/0004-6361/202346032, arXiv:2306.01834.

Markus, K., Arnold, G., Moroz, L. et al., 2024. Laboratory reflectance spectra of enstatite and oldhamite mixtures for comparison with E-type asteroids and implications for Mercury's surface composition analysis. In European Planetary Science Congress (pp. EPSC2024–446). URL: https://ui.adsabs.harvard.edu/abs/2024EPSC...17.446M. doi:10.5194/epsc2024-446.

Matsumoto, T., Tsuchiyama, A., Miyake, A. et al., 2015. Surface and internal structures of a space-weathered rim of an Itokawa regolith particle. Icarus, 257, 230–238. URL: https://ui.adsabs.harvard.edu/abs/2015Icar. 257.230M. doi:10.1016/j.icarus.2015.05.001.

Matsumoto, T., Tsuchiyama, A., Uesugi, K. et al., 2016. Nanomorphology of Itokawa regolith particles: Application to space-weathering processes affecting the Itokawa asteroid. Geochim. Cosmochim. Acta, 187, 195–217. URL: https://ui.adsabs.harvard.edu/abs/2016GeCoA.187.195M. doi:10.1016/j.gca.2016.05.011.

Matsuoka, M., Nakamura, T., Hiroi, T., et al., 2020. Space weathering simulation with low-energy laser irradiation of Murchison CM chondrite for reproducing micrometeoroid bombardments on c-type asteroids. ApJ 890 (2), L23. https://doi.org/10.3847/2041-8213/ab72a4.

Matsuoka, M., Nakamura, T., Kimura, Y., et al., 2015. Pulse-laser irradiation experiments of Murchison CM2 chondrite for reproducing space weathering on C-type asteroids. Icarus 254, 135–143. https://doi.org/10.1016/j.icarus.2015.02.029.

Matsuoka, M., Nakamura, T., Kimura, Y., et al., 2016. Reproducing space weathering on C-Type asteroids with low-energy laser irradiation experiments of the Murchison meteorite. In: 47th Annual Lunar and Planetary Science Conference Lunar and Planetary Science Conference, p. 1823, URL: https://ui.adsabs.harvard.edu/abs/2016LPI....47.1823M.

McAdam, M.M., Sunshine, J.M., Howard, K.T., et al., 2018. Spectral evidence for amorphous silicates in least-processed CO meteorites and their parent bodies. Icarus 306, 32–49. https://doi.org/10.1016/j.icarus.2018.01.024, arXiv:1802.00830.

Moretti, P.F., Maras, A., Folco, L., 2007. Space weathering, reddening and gardening of asteroids: a complex problem. Adv. Space Res. 40 (2), 258–261. https://doi.org/10.1016/j.asr.2007.04.022.

Moriarty, D.P., Pieters, C.M., 2016. Complexities in pyroxene compositions derived from absorption band centers: Examples from Apollo samples, HED meteorites, synthetic pure pyroxenes, and remote sensing data. Meteorit. Planet. Sci., 51(2), 207–234. URL: https://ui.adsabs.harvard.edu/abs/2016M&PS...51.207M. doi:10.1111/maps.12588.

Moyano-Cambero, C.E., Trigo-Rodríguez, J.M., Llorca, J., et al., 2016. A plausible link between the asteroid 21 Lutetia and CH carbonaceous chondrites. Meteorit. Planet. Sci. 51 (10), 1795–1812. https://doi.org/10.1111/maps.12703, arXiv:1607.01253.

Mozgai, V., Bajnóczi, B., Mráv, Z., et al., 2019. Application of a laboratory micro X-ray diffractometer (RIGAKU DMAX RAPID II) in the archaeometric analysis of archaeological artefacts - case studies of metal objects. Archeometriai Muhely 16, 29–42.

Nakamura, T., Matsumoto, M., Amano, K., et al., 2023. Formation and evolution of carbonaceous asteroid Ryugu: direct evidence from returned samples. Science 379 (6634), abn8671. https://doi.org/10.1126/science.abn8671.

Nasdala, L., Grambole, D., Götze, J., et al., 2010. Helium irradiation study on zircon. Contrib. Miner. Petrol. 161 (5), 777–789. https://doi.org/10.1007/s00410-010-0562-7.

Németh, P., 2021. Diffraction features from (10$\bar{1}$4) calcite twins mimicking crystallographic ordering. Minerals, 11(7), 720.https://ui.adsabs.harvard.edu/abs/2021Mine...11.720N. doi:10.3390/min11070720.

Németh, P., Lancaster, H.J., Salzmann, C.G. et al., 2022. Shock-formed carbon materials with intergrown sp^3- and sp^2-bonded nanostructured units. Proc. Natl. Acad. Sci., 119(30), e2203672119. URL: https://ui.adsabs.harvard.edu/abs/2022PNAS.11903672N. doi:10.1073/pnas.2203672119.

Noble, S.K., Pieters, C.M., Keller, L.P., 2007. An experimental approach to understanding the optical effects of space weathering. Icarus, 192(2), 629–642. URL: https://ui.adsabs.harvard.edu/abs/2007Icar.192.629N. doi:10.1016/j.icarus.2007.07.021.

Noguchi, T., Nakamura, T., Kimura, M. et al., 2011. Incipient space weathering observed on the surface of Itokawa dust particles. Science, 333(6046), 1121. URL: https://ui.adsabs.harvard.edu/abs/2011Sci...333.1121N. doi:10.1126/science.1207794.

Noval, V.E., Carriazo, J.G., 2019. Fe3O4-TiO2 and Fe3O4-SiO2 core-shell powders synthesized from industrially processed magnetite (Fe3O4) microparticles. Mater. Res. 22 (3). https://doi.org/10.1590/1980-5373-mr-2018-0660.

Németh, P., Mugnaioli, E., Gemmi, M., et al., 2018. A nanocrystalline monoclinic CaCO 3 precursor of metastable aragonite. Sci. Adv. 4 (12). https://doi.org/10.1126/sciadv.aau6178.

Pieters, C.M., He, G., Tompkins, S., 1996. Anorthosite and olivine layers of the farside upper crust at Tsiolkovsky. In: In Lunar and Planetary Science Conference (p. 1035). volume 27 of Lunar and Planetary Science Conference, URL: https://ui.adsabs.harvard.edu/abs/1996LPI....27.1035P.

Pieters, C.M., Klima, R.L., Hiroi, T. et al., 2008. Martian dunite NWA 2737: Integrated spectroscopic analyses of brown olivine. J. Geophys. Res. (Planets), 113(E6), E06004.https://ui.adsabs.harvard.edu/abs/2008JGRE.113.6004P. doi:10.1029/2007JE002939.

Pieters, C.M., Sunshine, J.M., Fischer, E.M. et al., 1993. Crustal diversity of the Moon: Compositional analyses of galileo solid state imaging data. J. Geophys. Res., 98(E9), 17127–17148.https://ui.adsabs.harvard.edu/abs/1993JGR....9817127P. doi:10.1029/93JE01221.

Pilorget, C., Okada, T., Hamm, V., et al., 2021. First compositional analysis of Ryugu samples by the MicrOmega hyperspectral microscope. Nat. Astron. 6, 221–225. https://doi.org/10.1038/s41550-021-01549-z.

Rupert, A.N., McCausland, P.J.A., Flemming, R.L., 2020. Ordinary chondrite shock stage quantification using in situ 2-D X-ray diffraction of olivine. Meteorit. Planet. Sci., 55(10), 2224–2240. URL: https://ui.adsabs.harvard.edu/abs/2020M&PS...55.2224R. doi:10.1111/maps.13572.

Sakuntala, T., Arora, A.K., Shekar, N.V.C., et al., 1998. Orientational disorder: a mechanism of amorphization at high pressure. Europhys. Lett. (EPL) 44 (6), 728–733. https://doi.org/10.1209/epl/i1998-00532-1.

Sasaki, S., Kurahashi, E., Yamanaka, C., et al., 2003. Laboratory simulation of space weathering: changes of optical properties and TEM/ESR confirmation of nanophase metallic iron. Adv. Space Res. 31 (12), 2537–2542. https://doi.org/10.1016/S0273-1177(03)00575-1.

Tanbakouei, S., Trigo-Rodríguez, J.M., Blum, J., et al., 2020. Comparing the reflectivity of ungrouped carbonaceous chondrites with those of short-period comets like 2P/Encke. A&A 641, A58. https://doi.org/10.1051/0004-6361/202037996, arXiv:2007.06212.

Tanbakouei, S., Trigo-Rodríguez, J.M., Sort, J., et al., 2019. Mechanical properties of particles from the surface of asteroid 25143 Itokawa. A&A 629, A119. https://doi.org/10.1051/0004-6361/201935380.

Thompson, M.S., Zega, T.J., Becerra, P. et al., 2016. The oxidation state of nanophase Fe particles in lunar soil: Implications for space weathering. Meteorit. Planet. Sci., 51(6), 1082–1095. https://ui.adsabs.harvard.edu/abs/2016M&PS...51.1082T. doi:10.1111/maps.12646.

Trigo-Rodríguez, J.M., 2022. Fireballs announcing meteorite falls. Asteroid Impact Risk: Impact Hazard from Asteroids and Comets. Springer International Publishing, Cham, pp. 1–19. https://doi.org/10.1007/978-3-030-95124-5_1, URL: https://doi.org/10.1007/978-3-030-95124-5_1.

Trigo-Rodríguez, J.M., Moyano-Cambero, C.E., Llorca, J., et al., 2014. UV to far-IR reflectance spectra of carbonaceous chondrites - I. Implications for remote characterization of dark primitive asteroids targeted by sample-return missions. MNRAS 437 (1), 227–240. https://doi.org/10.1093/mnras/stt1873, arXiv:1310.1742.

Urso, R.G., Vuitton, V., Danger, G. et al., 2020a. The composition of outer solar system icy surfaces: hints from the analysis of laboratory analogues. In: European Planetary Science Congress, pp. EPSC2020–135. doi:10.5194/epsc2020-135.

Urso, R.G., Vuitton, V., Danger, G. et al., 2020b. Irradiation dose affects the composition of organic refractory materials in space. Results from laboratory analogues. A&A, 644, A115. doi:10.1051/0004-6361/202039528. arXiv:2011.08650.

Wang, D., Fang, Y., Zhang, Y., et al., 2019. Changes in mineral composition, growth of calcite crystal, and promotion of physico-chemical properties induced by carbonation of β-C2S. J. CO2 Util. 34, 149–162. https://doi.org/10.1016/j.jcou.2019.06.005.

Weber, I., Böttger, U., Reitze, M.P., et al., 2023. Effects of simulated micrometeorite bombardment of rock-forming silicates in Raman spectra. In: 54th Lunar and Planetary Science Conference (p. 1134). volume 2806 of LPI Contributions, URL: https://ui.adsabs.harvard.edu/abs/2023LPICo2806.1134W.

Weber, I., Stojic, A.N., Morlok, A., et al., 2020. Space weathering by simulated micrometeorite bombardment on natural olivine and pyroxene: A coordinated IR and TEM study. Earth Planet. Sci. Lett. 530, 115884. https://doi.org/10.1016/j.epsl.2019.115884.

Yada, T., Abe, M., Okada, T., et al., 2021. Preliminary analysis of the Hayabusa2 samples returned from C-type asteroid Ryugu. Nat. Astron. 6, 214–220. https://doi.org/10.1038/s41550-021-01550-6.

Yakovenchuk, V.N., Pakhomovsky, Y.A., Panikorovskii, T.L., et al., 2019. Chirvinskyite, (Na, Ca)13(Fe, Mn,□)2(Ti, Nb)2(Zr, Ti)3-(Si2O7)4(OH, O, F)12, a new mineral with a modular wallpaper structure, from the khibiny alkaline massif (kola peninsula, russia). Minerals 9 (4), 219. https://doi.org/10.3390/min9040219.

Yang, Y., Zhang, H., Wang, Z., et al., 2016. Optical spectroscopic characterizations of laser irradiated olivine grains. Astron. Astrophys. 597, A50. https://doi.org/10.1051/0004-6361/201629327.